

Manganese Copper Sulfide Nanocomposites: Structure Tailoring and Photo/Electrocatalytic Hydrogen Generation

Jing Wang,^[a] Yee-Fun Lim,^[b] and Ghim Wei Ho^{*[a, b]}

In this paper, we present an L-cysteine-mediated hydrothermal synthesis of manganese copper sulfide (MCS) nanocomposites with versatile nanostructures and demonstrate their applications in photocatalytic and electrocatalytic hydrogen generation from water splitting. Variation of the Mn/Cu molar ratios in the precursors facily tailors the MCS nanocomposites into one-dimensional nanowires or two-dimensional nanosheets, which are different from the zero-dimensional nanoparticles of pure MnS and CuS. By virtue of the well-interfaced heterojunc-

tions formed, the recombination of photogenerated electrons and holes is suppressed, giving rise to photocatalytic hydrogen generation behavior that is unattainable from either MnS or CuS. Moreover, the electrochemical conductivity is dramatically enhanced, rendering the MCS nanocomposites with improved electrocatalytic kinetics. This approach will contribute to an inexpensive and convenient synthetic strategy of transition-metal-based nanostructures for functional applications in photovoltaic, electrochemical, and catalytic fields.

Introduction

Hybridization of two or more semiconducting nanomaterials into an entity of bi-/multiphase nanocomposites can bring about enhanced activities or even unique electrical, optical, and catalytic features that are usually unachievable from their respective constituents.^[1] In this regard, nanocomposites serving as prominent materials for applications in diverse fields, such as photocatalysis or electrocatalysis, can be adapted.^[2–4] The properties of the nanocomposites, from a fundamental point of view, are dominated by their chemical compositions, morphology contributions, and interfacial characteristics. Therefore, significant attempts have been devoted to the manipulation of their nanoscale structures in various dimensions so far. For instance, nanocomposites of higher dimensions often surpass zero-dimensional nanoparticles in specific surface area as well as mass and electron transport, thus resulting in more efficient catalytic behavior.^[5]

As an important VIII-VIA *p*-type semiconductor, manganese sulfide (MnS) exhibits excellent magneto-optical features that are meaningful for solar cells, photoconductors, and optoelectronic devices.^[6–8] However, the utilization of MnS-derived materials for the electrocatalytic generation of hydrogen, which is a clean and sustainable energy for the future, has rarely been reported to date. Moreover, owing to a large band gap of

3.7 eV, MnS responds mainly in the ultraviolet region (accounting for only 4–5% of the entire solar spectrum), which markedly restricts its light-harvesting capacity under solar irradiation.^[9,10] As a result, MnS fails to function independently as a photocatalyst for hydrogen evolution from water splitting. Integration with other component(s) to form well-defined nanocomposites, such as manganese cadmium sulfide (Mn_{1-x}Cd_xS) solid solutions, is able to endow MnS materials with good photoactivity.^[11–15] The concern of these cases is that the use of toxic cadmium element inevitably causes hazards to human beings and the environment, and CdS tends to photocorrode if exposed to illumination, making it impractical for long-term applications.^[16]

Herein, we report the first example of manganese copper sulfide (MCS) nanocomposites with diverse nanostructures through an L-cysteine-mediated hydrothermal synthesis, which are applied as effective photo- and electrocatalysts for hydrogen generation from water splitting. The integrated CuS not only deters the toxicity but also offers the nanocomposites with great durability, in contrast to its counterpart CdS. More importantly, the structures of these MCS nanocomposites can be facily tuned in zero-, one-, and two-dimension by simply adjusting the Mn/Cu molar ratios of the precursors. The well-interfaced heterojunctions formed between MnS and CuS are believed to accelerate the electron transfer, thus leading to enhanced photo-/electrocatalysis. The hybridization of semiconducting constituents into well-defined nanocomposites will advance the design of functional materials with controllable nanostructures and properties.

Results and Discussion

L-cysteine is an important amino acid involving three functional groups of mercapto (–SH), carboxyl (–COOH), and amine (–

[a] Dr. J. Wang, Prof. G. W. Ho
Department of Electrical and Computer Engineering
National University of Singapore
4 Engineering Drive 3, Singapore 117583 (Singapore)

[b] Dr. Y.-F. Lim, Prof. G. W. Ho
Institute of Materials Research and Engineering
A*STAR, Agency for Science, Technology and Research
2 Fusionopolis Way, Singapore 138634 (Singapore)
E-mail: elehwg@nus.edu.sg

Supporting information and the ORCID identification number(s) for the author(s) of this article can be found under <https://doi.org/10.1002/cctc.201700865>.

NH₂), which are capable of coordinating with a large number of metal cations to form “M-Cys” complexes in different binding modes and coordination geometries.^[17–19] The blending process of the Mn/Cu aqueous solution and L-cysteine is shown in Figure 1. The solution gradually evolves from pale

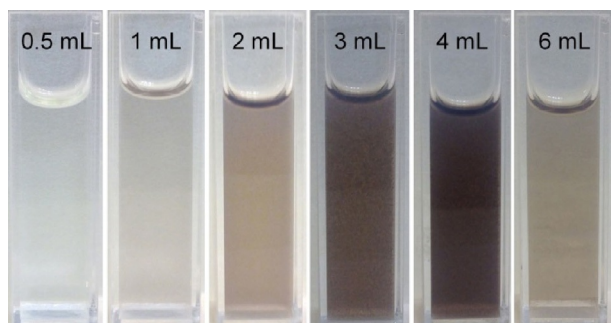


Figure 1. Photographs of the Mn/Cu solution blended with different volumes of L-cysteine solution.

yellowish (0.5 mL), brown (2 mL) to dark suspension (4 mL) as more L-cysteine is added, implying that this biomolecule readily bonds with the two metal ions. Further addition of L-cysteine causes a sudden color bleach to light brown and remains consistent thereafter, which is indicative of that the complexation is completed and the whole system is stabilized. The as-formed metal complexes subsequently undergo a mild hydrothermal treatment, by which L-cysteine releases extensive S²⁻ anions to react with the two metal cations, mediating the nucleation of MCS nanoparticles. These intermediates further grow larger and eventually self-assemble into MCS composites with varied nanostructures. L-cysteine here functions as (i) the capping ligand to stabilize the metal cations and (ii) the sulfur source to form hybrid metal sulfides.

The morphologies, particle-size distribution, and crystallinity of pure CuS and MnS, which are synthesized under identical hydrothermal conditions to that of MCS nanocomposites, are presented in Figure 2. As viewed from the low-magnification SEM images in Figure 2a,b, both CuS and MnS exhibit uniformly distributed nanoparticles exclusive of other nanostructures over a large area. The average particle diameters of CuS and MnS are regulated to be approximately 66 nm and 55 nm, respectively (insets of Figure 2a,b). The excessive L-cysteine, the sulfur source, is believed to restrict the anisotropic growth of the nanoparticles (the molar ratio of L-cysteine to metal cations is 4:1). In Figure 2c, the low-magnification TEM image of an individual CuS nanoparticle with smooth surface is given, which has a spherical shape of approximately 80 nm in diameter. Importantly, both CuS and MnS show favorable crystallinity as revealed by their HRTEM images in Figure 2d,e. The lattice spacings between each adjacent plane are observed to be 0.26 nm and 0.31 nm, corresponding to the (006) facet of CuS and the (102) facet of MnS, respectively.^[20,21] It is evident that the metal complexes are subjected to a bottom-up assembly and eventually agglomerate into nanoparticles during the template-free hydrothermal synthesis.

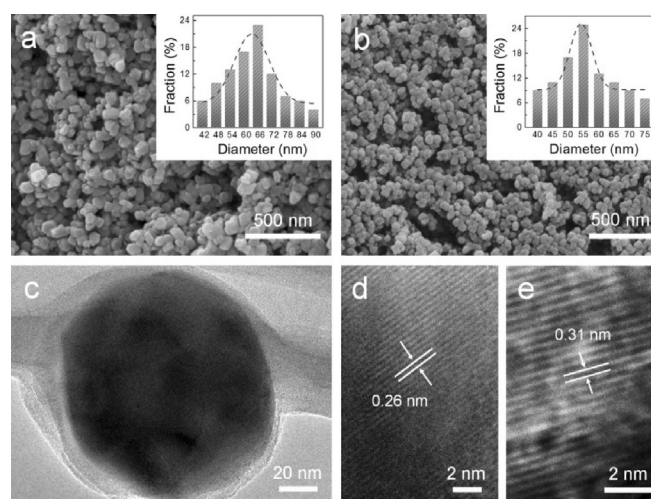


Figure 2. SEM images of (a) CuS and (b) MnS. Insets show their respective particle size distributions. (c) Low-magnification TEM image of CuS. HRTEM images of (d) CuS and (e) MnS.

Contrarily, MCS nanocomposites form versatile nanostructures that are markedly different from those of MnS and CuS. The morphologies of these MCS hybrids synthesized at different Mn/Cu molar ratios are displayed in Figure 3. At the Mn/Cu molar ratio of 1:1 (named as MCS-1), clusters of closely aggregated nanoparticles with a larger mean size of approximately 100 nm can be achieved (Figure 3a). As the molar ratio is enhanced to 3:1 (MCS-3), an ensemble of assembled ultrathin sheets is observed (Figure 3b), and further increase of the ratio to 5:1 (MCS-5) results in bunches of one-dimensional nanowires as thin as 45 nm (Figure 3c). If the molar ratio reaches 10:1 (MCS-10), a large amount of stacked two-dimensional nanoflakes are clearly seen (Figure 3d). Hence, the nanostructures of the MCS hybrids can be tailored by simply tuning the Mn/Cu molar ratios. We consider the formation of these nanostructures is associated with the coordination geometries of the metal complexes as well as the solubility products (K_{sp}) of

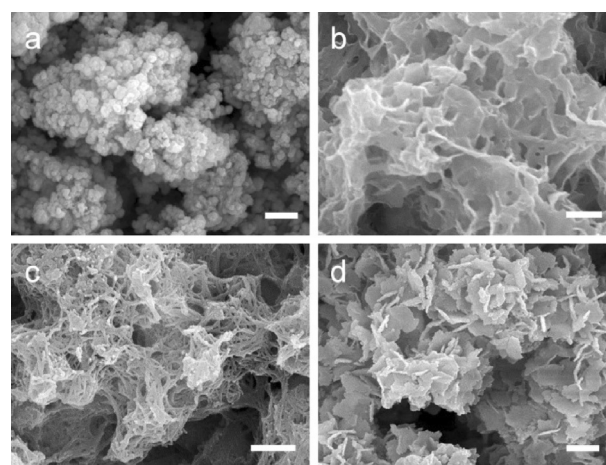


Figure 3. SEM images of MCS nanocomposites synthesized at different Mn/Cu molar ratios of (a) 1:1, (b) 3:1, (c) 5:1, and (d) 10:1. Scale bar: 500 nm.

the metal sulfides. Firstly, L-cysteine shows different binding behaviors with varied metal cations. According to the HSAB (hard soft acid base) principle of Parr and Pearson, the –SH group is considered as a soft base, and the other two groups (–COOH and –NH₂) hard bases. As a hard transition metal ion, Mn²⁺ ions disfavor the complexation with –SH group but prefer to couple with the latter two, giving rise to several energetically equal coordination structures. In contrast, the Cu²⁺ ion is regarded as a metal cation of intermediate hardness that has higher affinity with –SH groups, which results in tetrahedral or trigonal bipyramidal geometries.^[19] The two metal complexes in different binding configurations will determine the growth of their respective metal sulfides during the hydrothermal synthesis of the mixed system. Secondly, K_{sp} of MnS (2.5×10^{-13}) and CuS (6.3×10^{-36}) also play a key role in the formation of the nanocomposites.^[22] At the initial stage of the hydrothermal process, S²⁻ anions preferentially react with Cu²⁺ ions to yield less soluble CuS intermediate nuclei. However, Mn²⁺ ions that are higher in molar ratio (except MCS-1 that shows the morphology of nanoparticles) will competitively react with S²⁻ ions and affect the oriented nucleation of crystals,^[23] further modulating the nanocomposites into disparate structures.

To analyze the subtle structures of these MCS nanocomposites, TEM imaging of a representative MCS-3 was conducted. The clear structure of porous nanosheets is shown in Figure 4a, which is in concord with the SEM image in Figure 3b.

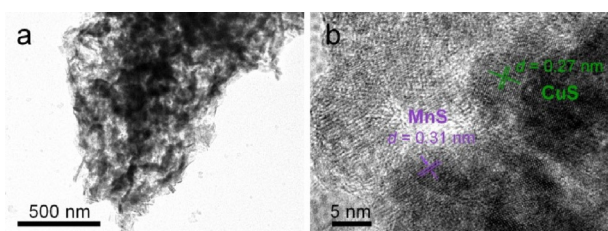


Figure 4. TEM images of MCS-3 at (a) low and (b) high magnifications.

Further examination of the lattice fringe reveals two interplanar distances of 0.31 nm and 0.26 nm (HRTEM image in Figure 4b), similar to the scenario of pure MnS and CuS, which can also be assigned to the (102) facet of MnS and (006) facet of CuS, respectively. This corroborates the successful hybridization of the two constituents in the nanocomposites. More importantly, closely interfaced heterojunctions are observed between MnS and CuS, which is considered to facilitate the electron transfer in the hybrid system.^[24–26]

The crystal structures of the MCS nanocomposites are explored by their powder XRD patterns, as compiled in Figure 5. The purple curve exhibits the diffraction peaks that can be indexed to hexagonal γ -MnS with wurtzite type (JCPDS card No.: 40-1289), and the green curve indicates the CuS with hexagonal covellite phase (JCPDS card No.: 06-0464). For the MCS nanocomposites, several characteristic peaks are present, including (102) planes from MnS and (103), (006), (110), and (116) planes from CuS, further confirming the MnS and CuS

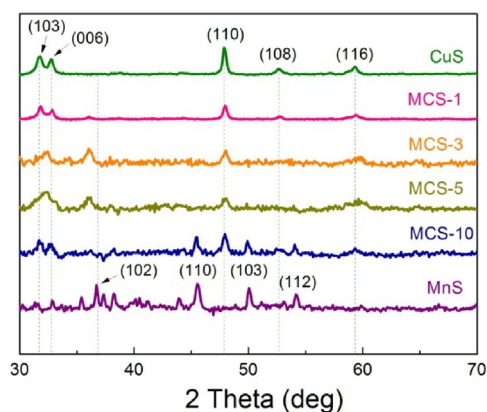


Figure 5. XRD patterns of MnS, CuS, and different MCS nanocomposites.

are well hybridized. The (102) phase of MnS ($2\theta = 36.3^\circ$) slightly shifts, which could be related to the changes in stoichiometry if more Cu is added into the system. Indeed, both of MnS and CuS exhibit hexagonal symmetry that may benefit phase amalgamation of the two constituents, thus resulting in thermodynamically stable nanocomposites.

Subsequently, the chemical compositions of the MCS nanocomposites are investigated. The energy-dispersive X-ray (EDX) spectra of pure MnS, CuS, and MCS-5 are shown in Figure 6a. The elemental analysis proves that MnS only consists of Mn and S elements, whereas CuS contains Cu and S with a tiny amount of O element. The presence of Mn, Cu, and S without other impurities is observed in MCS-5, which demonstrates the existence of MnS and CuS in the nanocomposites. These elements are found uniformly dispersed in the matrix of the nanocomposite (Figure S1, Supporting Information). The chemical information of MCS-5 is further understood by considering their chemical and electronic states, with the high-magnification X-ray photoelectron (XPS) spectra shown in Figure 6b–d. In the Mn2p region, the binding energies at 641.9 and 653.9 eV are ascribed to Mn2p_{3/2} and Mn2p_{1/2}, respectively, accompanied by a shake-up satellite peak at 648.7 eV. Two major peaks at 932.3 and 952.3 eV in the Cu2p region can be assigned to Cu2p_{3/2} and Cu2p_{1/2}, respectively. Compared to pure MnS and CuS (Figure S2 and S3), the peaks of Mn2p and Cu2p of MCS-5 shift approximately 0.5 eV, which could be resulted from the coupling of MnS and CuS. Meanwhile, the peaks located at 162.2 and 163.4 eV in the S2p region are attributed to S2p_{3/2} and S2p_{1/2}, respectively, indicating the divalent sulfide ions (S²⁻) in the composites. Collectively, MCS nanocomposites with versatile nanostructures tailored by different Mn/Cu molar ratios of the precursors have been successfully demonstrated.

The as-synthesized MCS nanocomposites can serve as effective photocatalysts and electrocatalysts for hydrogen generation from water splitting. Firstly, their photocatalytic performances are evaluated under a simulated solar irradiation, in which the Na₂S/Na₂SO₃ mixed solutions are used as the sacrificial agent. As shown in Figure 7a, the hydrogen generation rates of MCS nanocomposites are in the range of 25–50 $\mu\text{mol g}^{-1} \text{h}^{-1}$, and MCS-5 presents the highest photocatalytic

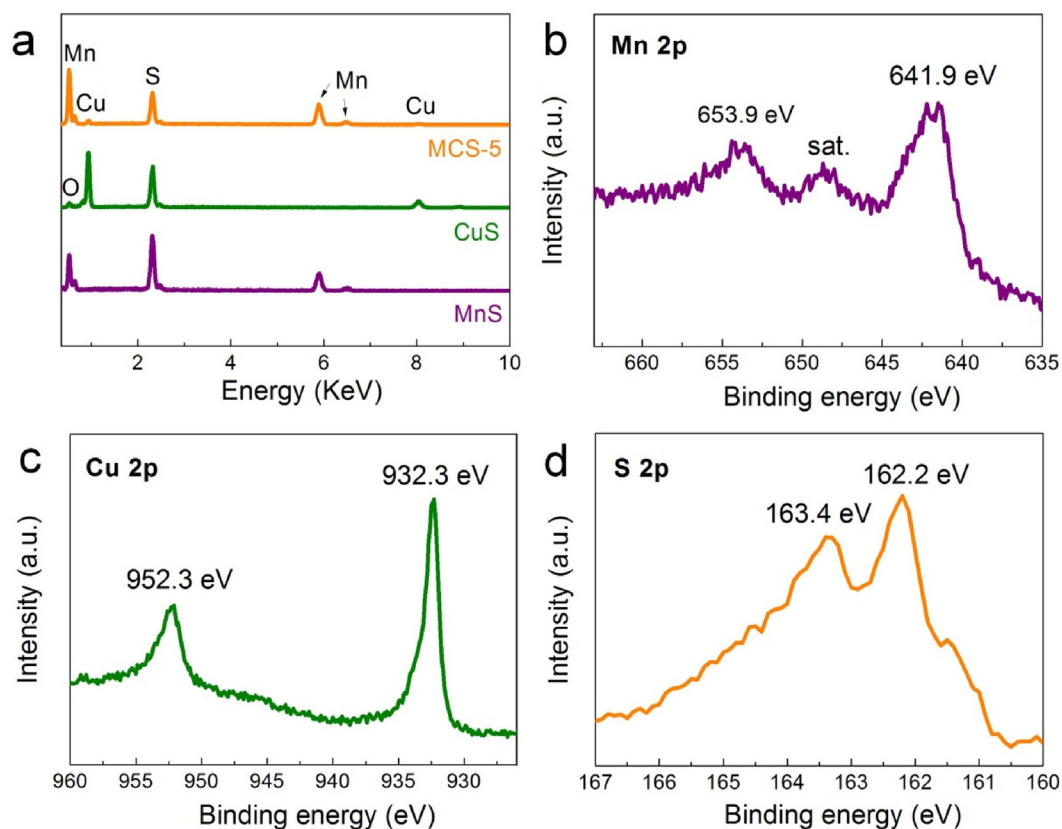


Figure 6. (a) EDX spectra of MnS, CuS, and MCS-5. (b) Mn 2p, (c) Cu 2p and (d) S 2p XPS spectra of MCS-5.

activity that should be related to the faster electron transfer along the one-dimensional thin nanowires.^[24] Unlike the reported sulfide semiconductors suffering from photocorrosion under continuous light illumination, MCS-5 shows consistent hydrogen production rates for several cycles (Figure 7b), indicating its great recyclability for long-term uses. Conversely, MnS and CuS are incapable of producing hydrogen independently under the same conditions. MnS is inferior in light harnessing because of its large band gap (3.7 eV), and the band-gap alignment of CuS with a valence band (VB) edge higher than the redox potential of O₂/H₂O (1.23 eV vs. normal hydrogen electrode, pH 0) does not meet the requirement for photocatalytic hydrogen generation. The biphasic heterojunctions in the MCS nanocomposites are considered to promote the interfacial charge transfer between the two components. The separation capacity of the photoinduced carriers can be determined by photoluminescence (PL) emission spectra.^[27] In Figure 7c, MCS-5 shows the lowest intensity of the PL emission centered at approximately 360 nm compared to MnS and CuS, suggesting the recombination of photoinduced electrons (e⁻) and holes (h⁺) pairs is suppressed. This hybridization of photoinactive semiconducting materials into nanocomposites with favorable photocatalytic behaviors will provide a new insight into the field of photocatalysis. The photocatalytic efficiency of these MCS nanocomposites is still undesirable; thus, several noble metals nanoparticles (Au, Ag, and Ru) were loaded onto MCS-5 by a simple photodeposition method. Their hydrogen

generation rates are displayed in Figure 7d. Au- and Ag-loaded MCS-5 succeed in generating hydrogen at enhanced rates of 91 and 110 μmol g⁻¹ h⁻¹, respectively, and the Ru-loaded one gives the highest value of 205 μmol g⁻¹ h⁻¹, which is 4 times higher than that of bare MCS-5. Notably, pure MnS and CuS deposited with the same metal nanoparticles still failed to produce hydrogen. As illustrated in Figure S4, CuS has a more positive conduction band (CB) and VB edges than MnS; hence, the electrons will be injected from the CB of CuS to MnS, and the holes generated in the VB of MnS will be transferred to CuS, which reduces the possibility of e⁻/h⁺ recombination. The metal loading drives the formation of a Schottky barrier at the MCS-5/metal interfaces, which will cause the electron transport from CB of MnS to the noble metals until a thermodynamic equilibrium state is reached.^[28] Accordingly, the e⁻/h⁺ pairs are further separated so that the electrons at the metal surfaces can capture protons to produce hydrogen for higher photoefficiency. Apart from photocatalytic hydrogen generation, these MCS nanocomposites can also promote the photodegradation of methyl orange (see details in Figure S5 in the Supporting Information).

Secondly, these MCS nanocomposites are coated onto nickel foams so as to form electrodes for electrocatalytic hydrogen evolution reactions (HER).^[29,30] The performances are considered by linear sweep voltammetry (LSV) curves measured in 1 M KOH electrolyte under room temperature, in which the current densities (*j*) are normalized by the geometric areas of elec-

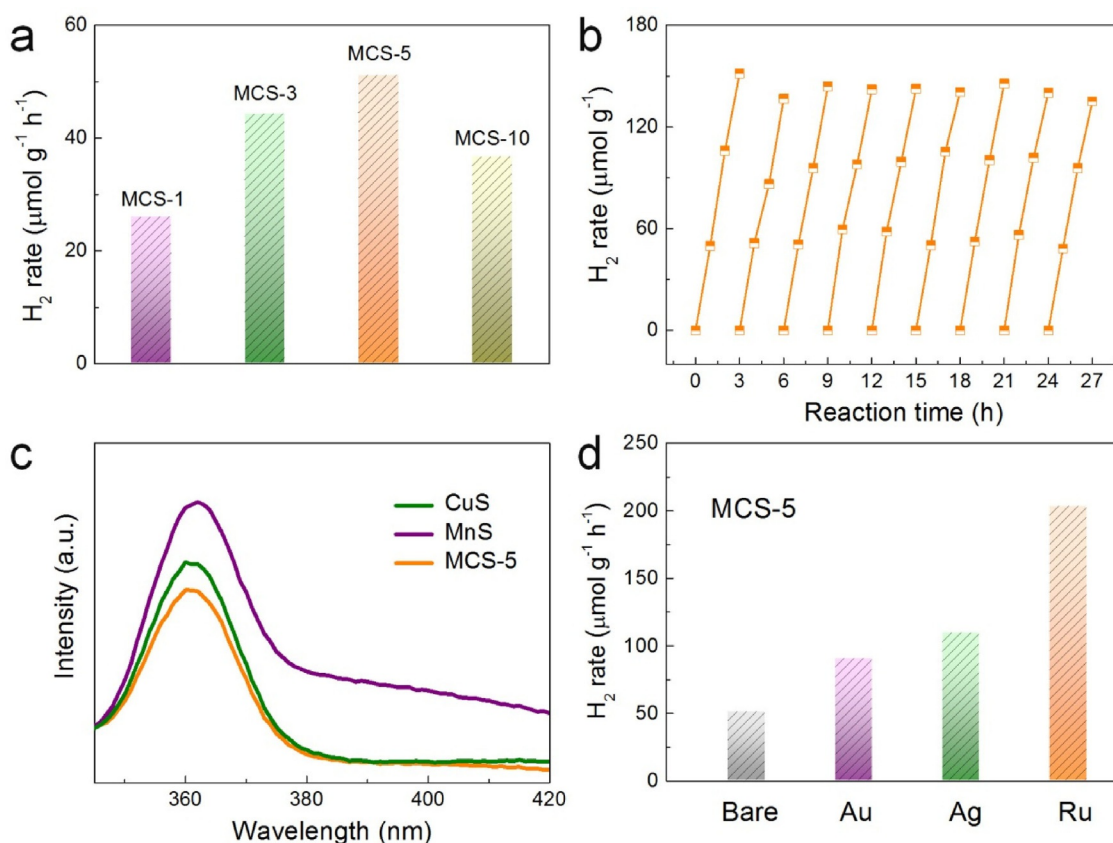


Figure 7. Hydrogen evolution of (a) different MCS nanocomposites and (b) MCS-5 for several cycles. (c) PL emission spectra of MnS, CuS, and MCS-5 aqueous solution ($\lambda_{\text{ex}}=320$ nm). (d) Hydrogen evolution of MCS-5 loaded with different noble-metal NPs (Au, Ag, and Ru).

trodes. As shown in Figure 8a, a typical MCS nanocomposite, that is, MCS-5, exceeds pure MnS and CuS in current densities across the applied potentials, demonstrating its superior HER responses. To reach the current density of 10 mA cm^{-2} , bare NF requires a large overpotential (η) of 250 mV whereas MCS-5 needs only 130 mV, much lower than the 175 mV of CuS and 181 mV of MnS. Moreover, the Tafel plots derived from $\log(j) \approx \eta$ fitted in Figure 8b show that MCS-5 has the smallest slope of 86 mV dec^{-1} , compared to 107 mV dec^{-1} of CuS and 144 mV dec^{-1} of MnS, further confirming its highest electrocatalytic kinetics towards hydrogen generation. The HER performance of MCS-5 is indeed comparable to recently reported metal-sulfide-based electrocatalysts measured in alkaline electrolytes (Table S2, Supporting Information). To understand the mechanism of the enhanced electrocatalytic activity, electrochemical impedance spectra (EIS) analysis of the three samples was performed. In Figure 8c, MCS-5 exhibits the smallest semi-circle diameter of approximately 250 ohm, indicating the lowest charge-transfer resistance. The integration of CuS with MnS in MCS nanocomposites enables accelerating the electron transfer between the two constituents to increase the electrochemical conductivity, thus promoting the electrocatalytic kinetics.^[31,32] Importantly, MCS-5 can retain $\approx 90\%$ of its current density after 16 h, as measured at the overpotential of 130 mV (Figure 8d), which demonstrates its practicability for sustainable applications.

Conclusions

A series of manganese copper sulfide (MCS) nanocomposites have been achieved by an L-cysteine-mediated hydrothermal synthesis. The alteration of the Mn/Cu molar ratios of the precursors enables a simple and efficient structural control in different dimensions. Compared to pure MnS or CuS that fail to produce hydrogen from photocatalytic water splitting, these nanocomposites can generate hydrogen gas at a rate up to $205 \mu\text{mol g}^{-1} \text{ h}^{-1}$. Furthermore, these MCS nanocomposites exhibit enhanced electrocatalytic hydrogen evolution reaction with a smaller overpotential of 130 mV and a Tafel slope of 86 mV dec^{-1} . The hybridization of different semiconducting constituents into bi-/multiphase nanocomposites will advance the design of transition-metal-based nanostructures for wide applications.

Experimental Section

Materials

Manganese chloride (MnCl_2), copper chloride (CuCl_2), L-cysteine ($\text{C}_3\text{H}_7\text{NO}_2\text{S}$), silver nitrate (AgNO_3), gold chloride trihydrate ($\text{HAuCl}_4 \cdot 3\text{H}_2\text{O}$), ruthenium chloride (RuCl_3), and Nafion solution were purchased from Sigma-Aldrich. All the chemicals were used as received without further purification. Nickel foams were purchased from standard sources. Before use, the foam was cut into

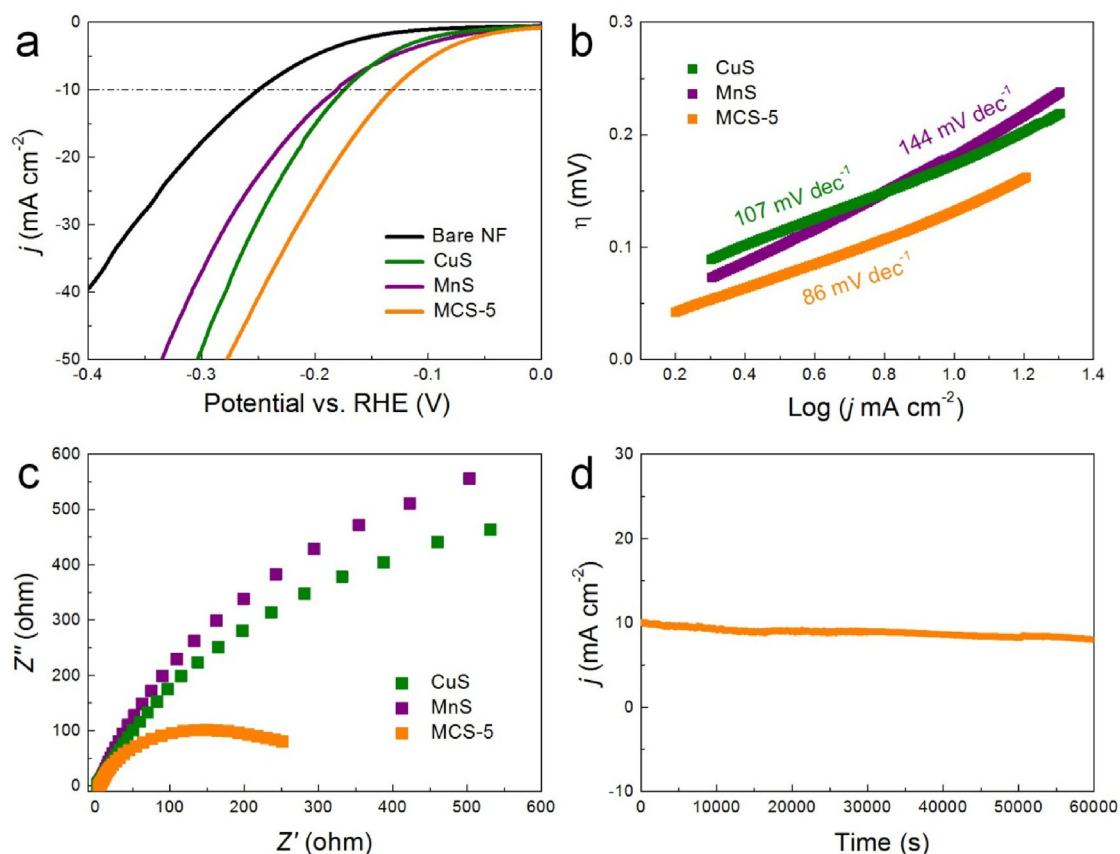


Figure 8. (a) LSV curves, (b) Tafel plots, and (c) EIS spectra of MnS, CuS, and MCS-5. (d) Time-dependent current density of MCS-5 measured at a static potential of 130 mV for 60000 s.

pieces (1 cm × 1.5 cm), rinsed successively with acetone, ethanol, and deionized water by ultrasonication, and finally blown-dry with nitrogen gas.

Synthesis of manganese copper sulfide (MCS) nanocomposites

Initially, L-cysteine (0.12 g) was dissolved in deionized (DI) water (10 mL), and the pH was adjusted to 10 by 1 M NaOH aqueous solution. Meanwhile, MnCl₂ (0.037 g) and CuCl₂ (0.008 g) were dissolved in DI water (25 mL) and stirred to form a homogenous solution. Afterwards, the as-prepared L-cysteine solution was added dropwise into the mixed Mn/Cu solution, and stirring was continued for 1 h under ambient conditions. The as-formed mixtures were transferred into a 50 mL Teflon-lined stainless-steel autoclave and maintained at 130 °C for 10 h. After cooling down to room temperature, the products were collected, centrifuged at 10000 rpm for 10 min and rinsed 3 times with DI water to remove the impurities. The precipitates were collected and dried at 60 °C for further use. The Mn/Cu molar ratios were 1:1 (MCS-1), 3:1 (MCS-3), 5:1 (MCS-5), and 10:1 (MCS-10), respectively. For comparison, pure MnS and CuS were also prepared under the same conditions, for which amounts of 0.05 g of MnCl₂ and 0.03 g of CuCl₂ were used, respectively.

Photocatalytic water splitting

An amount of 5 mg of MnS, CuS, or MCS nanocomposite powder was blended with a volume of 10 mL of Na₂S/Na₂SO₃ (0.35 M/0.25 M) solution in a cylindrical quartz vial, which was stirred for 30 min to form a homogeneous suspension. Before the photocatalytic water splitting, the suspensions were purged with Ar gas for 10 min. The measurements of H₂ production were performed by magnetically stirring the suspension under the illumination of a 300 W xenon arc lamp, in which the readings were taken every 1 h over 3 h. Noble metals were loaded onto the MCS nanocomposites by an in situ photoassisted deposition in concurrent with photocatalytic hydrogen evolution.^[33] Briefly, a 1 mL volume of the noble metal aqueous solution (3 wt %) was blended with the MCS-5 suspension and the mixture subjected to the illumination of a 300 W xenon arc lamp for 30 min.

Electrocatalytic water splitting

An amount of 5 mg of MnS, CuS, or MCS nanocomposite powder was dispersed in a volume of 0.5 mL of Nafion/ethanol (1:19 v/v) mixed solution by magnetic stirring for 30 min to form a uniform suspension. A piece of nickel foam was immersed into the suspension and dried at 60 °C for 1 h to form the electrode. The electrocatalysis was performed on a CHI 660D electrochemical work station, using 1 M KOH aqueous solution as the electrolyte. A three-electrode configuration was used, with the as-deposited nickel foam directly as the working electrode, a Pt foil as the counter electrode

and a saturated calomel electrode (SCE) as the reference electrode. Linear sweep voltammetry (LSV) curves were measured at a scan rate of 5 mVs^{-1} . Electrochemical impedance spectra (EIS) were recorded in the frequency range of 0.01 to 100 kHz with 5 mV amplitude. The current density versus time ($i-t$) curve was conducted at the overpotential of 130 mV for 60 000 s.

Characterizations

Scanning electron microscopy (SEM) images were obtained on a JEOL JSM-7001F field emission scanning electron microscope. High-resolution transmission electron microscopy (HRTEM) images were taken on a JEOL JEM-2100 electron microscope. X-ray diffraction (XRD) spectra of the powder samples were achieved on a Philips X-ray diffractometer with $\text{Cu}_{\text{K}\alpha}$ radiation ($\lambda = 1.541 \text{ \AA}$). Element analysis was performed on an Oxford Instruments energy dispersive X-ray (EDX) spectroscopy. X-ray photoelectron spectroscopy (XPS) spectra were attained on a VG Thermo Escalab 220I-XL system. UV/Vis absorption spectra were acquired on a Shimadzu UV-3600 UV/Vis spectrophotometer. Photoluminescence (PL) emission spectra were recorded on a Shimadzu RF-5301PC at an excitation wavelength of 320 nm. H_2 uptake was measured using pressure composition isotherm measurement on a Shimadzu GC-2014AT gas chromatographer.

Acknowledgements

This work is supported by MOE R-263-000-B38-112 and R-263-000-B63-112 (Ministry of Education, Singapore).

Conflict of interest

The authors declare no conflict of interest.

Keywords: copper · electrochemistry · manganese · nanostructures · water splitting

- [1] M. Ibáñez, Z. Luo, A. Genç, L. Piveteau, S. Ortega, D. Cadavid, O. Dobrozhani, Y. Liu, M. Nachttegaal, M. Zebarjadi, J. Arbiol, M. V. Kovalenko, A. Cabot, *Nat. Commun.* **2016**, *7*, 10766.
- [2] N. Zhang, M.-Q. Yang, S. Liu, Y. Sun, Y.-J. Xu, *Chem. Rev.* **2015**, *115*, 10307–10377.
- [3] Q. Lu, Y. Yu, Q. Ma, B. Chen, H. Zhang, *Adv. Mater.* **2016**, *28*, 1917–1933.
- [4] M. Wang, J. Iocozia, L. Sun, C. Lin, Z. Lin, *Energy Environ. Sci.* **2014**, *7*, 2182–2202.
- [5] B. Luo, G. Liu, L. Wang, *Nanoscale* **2016**, *8*, 6904–6920.

- [6] F. Zuo, B. Zhang, X. Tang, Y. Xie, *Nanotechnology* **2007**, *18*, 215608.
- [7] J. Lu, P. Qi, Y. Peng, Z. Meng, Z. Yang, W. Yu, Y. Qian, *Chem. Mater.* **2001**, *13*, 2169–2172.
- [8] K. Qi, R. Selvaraj, U. Jeong, S. M. Z. Al-Kindy, M. Sillanpaa, Y. Kim, C.-W. Tai, *RSC Adv.* **2015**, *5*, 9618–9620.
- [9] M.-Q. Yang, N. Zhang, M. Pagliaro, Y.-J. Xu, *Chem. Soc. Rev.* **2014**, *43*, 8240–8254.
- [10] J. Hu, A. Liu, H. Jin, D. Ma, D. Yin, P. Ling, S. Wang, Z. Lin, J. Wang, *J. Am. Chem. Soc.* **2015**, *137*, 11004–11010.
- [11] K. Ikeue, S. Shiiba, M. Machida, *Chem. Mater.* **2010**, *22*, 743–745.
- [12] K. Ikeue, S. Shiiba, M. Machida, *ChemSusChem* **2011**, *4*, 269–273.
- [13] M. Liu, Y. Du, L. Ma, D. Jing, L. Guo, *Int. J. Hydrogen Energy* **2012**, *37*, 730–736.
- [14] K. Ikeue, Y. Shinmura, M. Machida, *Appl. Catal. B* **2012**, *123*, 84–88.
- [15] M. Liu, L. Zhang, X. He, B. Zhang, H. Song, S. Li, W. You, *J. Mater. Chem. A* **2014**, *2*, 4619–4626.
- [16] M.-Q. Yang, C. Han, Y.-J. Xu, *J. Phys. Chem. C* **2015**, *119*, 27234–27246.
- [17] A. Manceau, C. Lemouchi, M. Enescu, A.-C. Gaillot, M. Lanson, V. Magnin, P. Glatzel, B. A. Poulin, J. N. Ryan, G. R. Aiken, I. Gautier-Luneau, K. L. Nagy, *Environ. Sci. Technol.* **2015**, *49*, 9787–9796.
- [18] Z. Luo, X. Yuan, Y. Yu, Q. Zhang, D. T. Leong, J. Y. Lee, J. Xie, *J. Am. Chem. Soc.* **2012**, *134*, 16662–16670.
- [19] H. Pesonen, R. Aksela, K. Laasonen, *J. Phys. Chem. A* **2010**, *114*, 466–473.
- [20] S. Lei, K. Tang, Q. Yang, H. Zheng, *Eur. J. Inorg. Chem.* **2005**, 4124–4128.
- [21] H. Wu, W. Chen, *Nanoscale* **2011**, *3*, 5096–5102.
- [22] J. Wang, G. W. Ho, *Angew. Chem.* **2015**, *127*, 16030–16034.
- [23] F. Zuo, S. Yan, B. Zhang, Y. Zhao, Y. Xie, *J. Phys. Chem. C* **2008**, *112*, 2831–2835.
- [24] J. Wang, M. Gao, G. W. Ho, *J. Mater. Chem. A* **2014**, *2*, 5703–5709.
- [25] C. Mondal, A. Singh, R. Sahoo, A. K. Sasmal, Y. Negishi, T. Pal, *New J. Chem.* **2015**, *39*, 5628–5635.
- [26] H. Wang, L. Zhang, Z. Chen, J. Hu, S. Li, Z. Wang, J. Liu, X. Wang, *Chem. Soc. Rev.* **2014**, *43*, 5234–5244.
- [27] M. Ye, J. Gong, Y. Lai, C. Lin, Z. Lin, *J. Am. Chem. Soc.* **2012**, *134*, 15720–15723.
- [28] C.-T. Dinh, H. Yen, F. Kleitz, T.-O. Do, *Angew. Chem. Int. Ed.* **2014**, *53*, 6618–6623; *Angew. Chem.* **2014**, *126*, 6736–6741.
- [29] Y. C. Hu, Y. Z. Wang, R. Su, C. R. Cao, F. Li, C. W. Sun, Y. Yang, P. F. Guan, D. W. Ding, Z. L. Wang, W. H. Wang, *Adv. Mater.* **2016**, *28*, 10293–10297.
- [30] Y. Gong, Y. Zhao, Y. Chen, Y. Wang, C. Sun, *RSC Adv.* **2016**, *6*, 43185–43190.
- [31] H. Wu, J. Geng, H. Ge, Z. Guo, Y. Wang, G. Zheng, *Adv. Energy Mater.* **2016**, *6*, 1600794.
- [32] J. Wang, W. Cui, Q. Liu, Z. Xing, A. M. Asiri, X. Sun, *Adv. Mater.* **2016**, *28*, 215–230.
- [33] W. Y. Lim, M. Hong, G. W. Ho, *Dalton Trans.* **2016**, *45*, 552–560.

Manuscript received: May 26, 2017

Revised manuscript received: June 8, 2017

Accepted manuscript online: June 9, 2017

Version of record online: October 18, 2017